

The evolution of the [O II], H β and [O III] emission-line luminosity functions over the last nine billions years

Johan Comparat^{1,2*}†, Guangtun Zhu³, Violeta Gonzalez-Perez^{4,5}, Peder Norberg⁵, Jeffrey Newman⁶, Laurence Tresse⁸, Johan Richard⁸, Gustavo Yepes², Jean-Paul Kneib⁹, Anand Raichoor¹⁰, Francisco Prada¹, Claudia Maraston⁴, Christophe Yèche¹⁰, Timothée Delubac⁹, Eric Jullo⁷.

¹*Instituto de Física Teórica UAM/CSIC, 28049 Madrid, Spain*

²*Departamento de Física Teórica, Universidad Autónoma de Madrid, 28049 Madrid, Spain*

³*Department of Physics & Astronomy, Johns Hopkins University, 3400 N. Charles Street, Baltimore, MD 21218, USA*

⁴*Institute of Cosmology and Gravitation, University of Portsmouth, Portsmouth, PO1 3FX, UK*

⁵*Institute for Computational Cosmology and Centre for Extragalactic Astronomy, Department of Physics, University of Durham, South Road, Durham, DH1 3LE, U.K.*

⁶*Department of Physics and Astronomy and PITT PACC, University of Pittsburgh, Pittsburgh, PA 15260, USA*

⁷*Aix Marseille Université, CNRS, LAM (Laboratoire d'Astrophysique de Marseille) UMR 7326, F-13388, Marseille, France*

⁸*Univ Lyon, Univ Lyon 1, Ens de Lyon, CNRS, Centre de Recherche Astrophysique de Lyon UMR5574, F-69230, Saint-Genis-Laval, France*

⁹*Laboratoire d'Astrophysique, Ecole Polytechnique Fédérale de Lausanne (EPFL), Observatoire de Sauverny, CH-1290 Versoix, Switzerland*

¹⁰*CEA, Centre de Saclay, IRFU/SPP, F-91191 Gif-sur-Yvette, France*

October 15, 2018

ABSTRACT

Emission line galaxies are one of the main tracers of the large-scale structure to be targeted by the next-generation dark energy surveys. To provide a better understanding of the properties and statistics of these galaxies, we have collected spectroscopic data from the VVDS and DEEP2 deep surveys and estimated the galaxy luminosity functions (LFs) of three distinct emission lines, [O II] ($\lambda\lambda 3726, 3729$) ($0.5 < z < 1.3$), H β ($\lambda 4861$) ($0.3 < z < 0.8$) and [O III] ($\lambda 5007$) ($0.3 < z < 0.8$). Our measurements are based on 35,639 emission line galaxies and cover a volume of $\sim 10^7 \text{Mpc}^3$. We present the first measurement of the H β LF at these redshifts. We have also compiled LFs from the literature that were based on independent data or covered different redshift ranges, and we fit the entire set over the whole redshift range with analytic Schechter and Saunders models, assuming a natural redshift dependence of the parameters. We find that the characteristic luminosity (L_*) and density (ϕ_*) of all LFs increase with redshift. Using the Schechter model over the redshift ranges considered, we find that, for [O II] emitters, the characteristic luminosity $L_*(z = 0.5) = 3.2 \times 10^{41} \text{erg} \cdot \text{s}^{-1}$ increases by a factor of 2.7 ± 0.2 from $z=0.5$ to 1.3 ; for H β emitters $L_*(z = 0.3) = 1.3 \times 10^{41} \text{erg} \cdot \text{s}^{-1}$ increases by a factor of 2.0 ± 0.2 from $z=0.3$ to 0.8 ; and for [O III] emitters $L_*(z = 0.3) = 7.3 \times 10^{41} \text{erg} \cdot \text{s}^{-1}$ increases by a factor of 3.5 ± 0.4 from $z=0.3$ to 0.8 .

Key words: catalogues - surveys - galaxies: abundances - galaxies: evolution - galaxies: general - cosmology: observations.

1 INTRODUCTION

Recent precise observations of the cosmic microwave background, the supernovae, and the Cepheids at the two ends of the observable Universe ($z \sim 1100$ and $z \sim 0$) has led to the Λ CDM concordance model (e.g., Freedman & Madore

2010; Planck Collaboration et al. 2014; Suzuki et al. 2012). It successfully describes the evolution of the homogeneous Universe, though requires exotic elements such as dark matter and dark energy (e.g., Frieman et al. 2008).

For a better understanding of the puzzling dark ingredients, it is important to investigate what happened between the two ends and measure directly the expansion history of the Universe.

Observations now revolve around the inhomogeneous

* j.comparat@csic.es

† Severo Ochoa IFT Fellow

Universe, in particular, by using the baryon acoustic oscillation (BAO) as a standard ruler (e.g., Cole et al. 2005; Eisenstein et al. 2005). The Baryonic Oscillation Spectroscopic Survey (BOSS) experiment demonstrated the ability of BAO measurements to provide a standard ruler to the percent level at redshift 0.5 (Anderson et al. 2014). Though the BAO is known to be largely free of systematic errors (e.g., Vargas-Magaña et al. 2014; Ross et al. 2015), precise measurement requires surveys of a large number of sources over a large cosmic volume. The current and future dark-energy surveys aim to efficiently sample tens of millions of faint galaxies/quasars at redshift $0.5 \lesssim z \lesssim 2.3$ over the entire observable sky to measure BAO at the percent level (e.g. eBOSS¹, DESI², PFS³, 4MOST⁴, *EUCLID*⁵).

The eBOSS survey (?) in the SDSS-IV (Blanton et al., in preparation), started in Fall 2014 and is currently mapping the large-scale structure at redshift $z > 0.6$ with four different tracers: luminous red galaxies (LRGs, Prakash et al. 2015), emission line galaxies (ELGs, Comparat et al. 2015a), QSOs, and Lyman α absorption (Myers et al. 2015; Palanque-Delabrouille et al. 2016). It will provide the first density map covering the redshift range $0.6 < z < 2.5$ over a large portion of the sky (7,500 deg² of LRGs and QSOs, 1,500 deg² of ELGs).

To achieve these goals with a 2.5-metre telescope, eBOSS requires efficient methods to pre-select targets using both magnitude and colour cuts. For ELGs, there is an additional source of complication: their redshifts will be mainly determined by emission lines, and it is therefore important to characterize the sampling efficiency of ELGs with broadband magnitude and colour selections (e.g. Comparat et al. 2015a; Raichoor et al. 2016). Studies have shown that the future ELG surveys will sample the [O II] or the H α emitters in an incomplete manner (Comparat et al. 2015b; Tonegawa et al. 2015). A more precise quantification of this incompleteness is critical for a more detailed understanding of the selection effects and to enable more precise cosmological analysis.

In the redshift range targeted by eBOSS ($0.6 < z < 1.2$ for ELGs), the strongest emission-lines that can be observed in the optical are the oxygen [O II] ($\lambda\lambda 3726, 3729$), [O III] ($\lambda 5007$) lines and the hydrogen H β ($\lambda 4861$) Balmer line. All other lines are either outside of the optical window at these redshifts, or an order of magnitude weaker and therefore will not drive the completeness of the ELG survey. Of these three line luminosity functions (LFs), the [O II] LF is the most well-known. Its LF has been measured from redshift 0 to 4.7 (e.g., Ly et al. 2007; Zhu et al. 2009; Gilbank et al. 2010; Bayliss et al. 2011; Sobral et al. 2012; Comparat et al. 2015b; Khostovan et al. 2015), mostly due to interests in using [O II] as an empirical star formation rate (SFR) indicator (see Kennicutt 1998; Kewley et al. 2004; Moustakas et al. 2006). The [O III] and H β LFs have been studied between redshift 0 and 3.3 mostly with narrow-band imaging and are usually measured together (including [O III] $\lambda 4959$) as a single LF due to the low spectral resolution (e.g., Ly

et al. 2007; Drake et al. 2013; Khostovan et al. 2015; Sobral et al. 2015). Over the redshift range we are interested in, we did not find a measurement of the H β ($\lambda 4861$) LF alone (without [O III]).

We present here independent measurements of the [O II] ($\lambda\lambda 3726, 3729$) (total luminosity in the two lines), H β ($\lambda 4861$) and [O III] ($\lambda 5007$) ([O III] ($\lambda 4959$) is not included) LFs, by taking advantage of the large spectroscopic data sets made available by recent deep surveys, the Visible MultiObject Spectrograph Very Large Telescope Deep Survey⁶ (VVDS) and the DEEP2 survey⁷ (Le Fèvre et al. 2013; Newman et al. 2013, respectively). In addition, we fit the observed LF with two models, the Schechter function (Schechter 1976) and the Saunders function (Saunders et al. 1990) over the entire redshift range.

Throughout the paper, we use AB magnitudes (Oke & Gunn 1982) and provide measurements in a flat Λ CDM cosmology ($h = 0.677$, $\Omega_{m0} = 0.307$; Planck Collaboration et al. 2014).

Spectra, catalogues, LFs, code and fitting functions are publicly available through the skies and universes data base.⁸

2 DATA

From the VVDS and DEEP2 survey data bases, we collected spectra of 69,529 unique galaxies with a reliable redshift $z > 0.1$. Among them, 35,639 have at least one emission line with signal to noise ratio (SNR) greater than 5. We present the summary of the data sets in Table 1 and describe each data set in Sections 2.1 and 2.2. We detail the procedure of emission line fitting in Section 2.3 and give the line flux completeness in Section 2.4.

2.1 VVDS

VVDS (Le Fèvre et al. 2013) was conducted with the visible wide field imager and multi-object spectrograph (VIMOS) mounted on the Nasmyth focus B of UT3 Melipal of the European Southern Observatory Very Large Telescope located in Chile (Le Fèvre et al. 2003). VVDS is a magnitude-limited survey and includes a Wide component and a Deep component. The magnitude limits are $i = 22.5$ and 24.0 and the effective areas covered are 5.8 and 0.6 deg² for the Wide and the Deep, respectively. The targets were chosen using the i magnitude from CFHT observations (McCracken et al. 2003; Ilbert et al. 2005; Cucciati et al. 2012). The VVDS collaboration provides the slit-extracted 1D-spectra and the redshift catalogue based on visual inspection of the spectra. The spectral resolution \mathcal{R} is about ~ 230 and the wavelength coverage is from 550 to 935 nm. The exposure time ranges from 0.75 h for the Wide to 4.5 h for the Deep. Further information on VVDS may be found in Le Fèvre et al. (2013). We obtain 5,909 and 3,833 ELGs with at least one of the three [O II], H β and [O III] lines with $\text{SNR} > 5$ in the VVDS-Wide and VVDS-Deep fields, respectively.

¹ <http://sdss.org/>

² <http://desi.lbl.gov/>

³ <http://sumire.ipmu.jp/>

⁴ <https://www.4most.eu/>

⁵ <http://sci.esa.int/euclid/>

⁶ <http://cesam.lam.fr/vvdspub/>

⁷ <http://deep.ps.uci.edu/>

⁸ <http://projects.ift.uam-csic.es/skies-universes/>

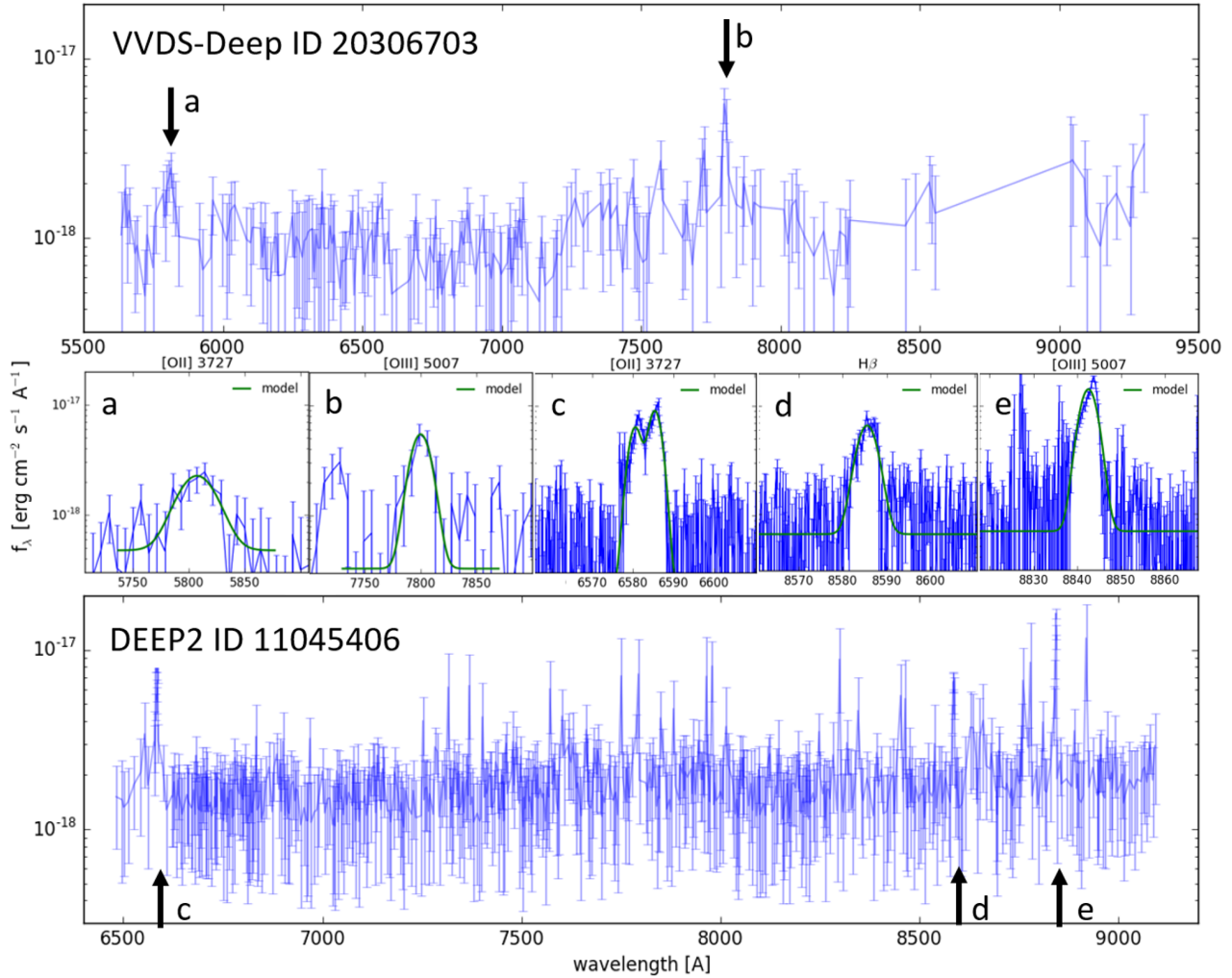


Figure 1. Typical VVDS-Deep (top row) and DEEP2 (bottom row) spectra processed with the emission line pipeline. The observed spectrum is shown in blue error bars. We show only points with an SNR larger than 1.5 (DEEP2) and 1.2 (VVDS), otherwise the plot would be dominated by noise. For the DEEP2 spectrum we only show every five points. In the middle row of panels, we show a zoom on the emission lines found in each spectra (no filtering, all data points are shown) and their best-fitting model (green solid line). The VVDS-Deep galaxy (ID 20306703) has a magnitude $i=23.9$ and a redshift $z=0.55$. The DEEP2 galaxy spectrum (ID 11045406) has a magnitude $R=23.7$ and a redshift $z=0.76$. The DEEP2 spectrum is shown after applying flux calibration. The VVDS spectrum shown is corrected from aperture, the emission line fits, performed before correction are plotted along with the uncorrected spectrum.

Table 1. The spectroscopic data. The total sample contains 69,529 unique galaxy spectra and among them 35,639 with emission-lines. The effective (non-masked) area is given in the second column. We give the magnitude cut applied in each survey in the column ‘mag. limit’ and provide the bands eventually used for a colour selection in the column ‘colour selection’. The \mathcal{R} and λ columns give the resolution at the median wavelength and the wavelength range covered by the spectrographs. N_{total} is the number of galaxies with an estimated redshift at $z > 0.1$ (VVDS: $Z_{\text{flags}} \geq 1$, DEEP2: $Z_{\text{QUALITY}} \geq 2$). N_{lines} is the subset of galaxies for which at least one of the [O II] or H β or [O III] lines has a SNR > 5 . All 35,639 with emission-lines have redshift quality flags VVDS: $Z_{\text{flags}} \geq 2$, DEEP2: $Z_{\text{QUALITY}} \geq 3$.

Survey	Area (deg ²)	Mag. limit	colour selection	\mathcal{R}	λ (nm)	N_{total}	N_{lines} ([O II]; H β ; [O III])
VVDS-Deep	0.6	$i_{\text{AB}} < 24$	No	230	550 935	10,123	3,833 (2,853; 472; 1,226)
VVDS-Wide	5.8	$i_{\text{AB}} < 22.5$	No	230	550 935	23,993	5,909 (3,652; 911; 2,334)
DEEP2 Field 1 (EGS)	0.5	$R_{\text{AB}} < 24.1$	No	6000	640 910	12,263	8,374 (4,444; 3,202; 4,144)
DEEP2 Fields 2, 3, 4	3.0	$R_{\text{AB}} < 24.1$	BRI	6000	640 910	23,140	17,523 (15,358; 3,800; 3,364)

2.2 DEEP2

DEEP2 (Newman et al. 2013) was conducted with DEep Imaging Multi-Object Spectrograph (DEIMOS; Faber et al. 2003) mounted on the Nasmyth focus of the Keck II telescope. In DEEP2 Fields 2, 3, 4, the survey is complete down to $R = 24.1$ at redshift $z > 0.7$, with the desired redshift range achieved with a pre-selection on the $B - R$ and $R - I$ plane, while Field 1 (the Extended Groth Strip, EGS) did not include the colour pre-selection and is complete over the entire redshift range ($0 < z \lesssim 1.4$). DEEP2 is a complete galaxy survey for redshifts $z > 0.7$ and magnitude $R \leq 24.1$. The DEEP2 collaboration released redshift catalogues and 1D slit-extracted spectra. The spectral resolution \mathcal{R} is about 6000 and the wavelength coverage is from 640 to 910 nm. Further information on DEEP2 may be found in Newman et al. (2013). We obtain 25,897 ELGs from the DEEP2 data.

2.3 From spectra to emission line catalogues

We first construct catalogues of emission lines based on the spectra and redshift catalogues provided by the aforementioned surveys. We use a single routine to fit the flux of emission lines in the galaxy spectra across the different surveys, inspired by the SDSS pipeline (Bolton et al. 2012; Thomas et al. 2013). As the resolution varies from one survey to another, $\mathcal{R} \sim 230$ for VVDS and ~ 6000 for DEEP2, we cannot extract the same level of information from all the spectra and our code includes free parameters to treat properly the different resolutions. In this paper, although we focus on the [O II] ($\lambda\lambda 3726, 3729$) (sum of the two lines), H β ($\lambda 4861$) and [O III] ($\lambda 5007$) (note that [O III] ($\lambda 4959$) is not included) lines, we extend the search to a series of lines for future analysis. Table 2 summarizes the list of emission lines we search for in each spectrum. To avoid the contamination from the strong sky lines in the red, we only search for lines up to $\lambda = 9000 \text{ \AA}$.

Our emission-line measurement pipeline includes the following steps.

(i) Flux-calibrate the DEEP2 spectra. As the spectra given by the DEEP2 collaboration are not flux-calibrated, we perform the calibration ourselves with the broad-band photometry. The calibration procedures includes the following items.

(a) The correction of the quantum efficiency of the detector chips.

(b) The correction of the A and B telluric absorption bands.

(c) The flux calibration using the R and I total photometry, assuming that the shape of the observed spectrum within the slit is representative of that of the spectral energy distribution (SED) emitted by the whole galaxy.

(ii) The correction of aperture effects of the VIMOS spectra. The slit spectra from VVDS are already calibrated for spectrophotometry. We apply additional aperture corrections to convert the flux within the slit to the total flux of the whole galaxy:

(a) Integrate the observed spectrum over the i -band filter (which is the selection band of the survey),

Table 2. The list of emission lines searched for in the spectra, with wavelengths collected from Luridiana et al. (2015). We split the lines into collisional and recombination groups. The last column gives the redshift where the line’s observer-frame wavelength is 9000 \AA , the maximum wavelength considered in the line identification. We quote wavelengths in the air (for VVDS, DEEP2, VIPERS) and in the vacuum (for SDSS) because surveys provide spectra wavelengths in one of the conventions but not both.

Line	Rest-frame wavelength [\AA]		z at 9000 \AA
	vacuum	air	
Collisional lines			
[O II]	3727.092	3726.032	1.41
[O II]	3729.875	3728.815	1.41
[Ne III]	3869.861	3868.764	1.32
[O III]	4364.436	4363.209	1.06
[O III]	4960.295	4958.910	0.81
[O III]	5008.240	5006.842	0.79
[N II]	6549.861	6548.049	0.37
[N II]	6585.273	6583.451	0.36
[S II]	6718.295	6716.437	0.34
[S II]	6732.674	6730.812	0.33
Recombination lines			
H ϵ	3971.202	3970.079	1.26
H δ	4102.899	4101.741	1.19
H γ	4341.691	4340.470	1.07
H β	4862.691	4861.332	0.85
H α	6564.632	6562.816	0.37

$$m_{\text{spec}} = \frac{\int_{\text{broad-band}} d\lambda f_{\lambda}(\lambda) \text{filter}(\lambda)}{\int_{\text{broad-band}} d\lambda \text{filter}(\lambda)} ; \quad (1)$$

(b) Convert the m_{spec} into AB magnitude $m_{\text{spec, AB}}$ and compare $m_{\text{spec, AB}}$ with the total magnitude taken from the targeting photometry, assuming the shape of the observed spectrum within the slit represents that of the total SED of the whole galaxy.

(iii) Determine the observer frame wavelength of the emission lines listed, denoted $\bar{\lambda}$, listed in Table 2 using the best redshifts from the catalogues.

(iv) Estimate the continuum flux density $C_{\bar{\lambda}}$ (in $\text{erg} \cdot \text{s}^{-1} \cdot \text{cm}^{-2} \cdot \text{\AA}^{-1}$), using the median of the observed spectrum in a wide (dependent on the resolution) spectral band on the left-hand side or on the right-hand side of the expected line location.

(v) Compare the mean flux density in the two closest pixels to the expected line position with the flux density of the continuum ($C_{\bar{\lambda}}$). If this ratio is greater than one, we fit a line model.

(vi) Fit each line with a Gaussian model:

$$f_{\bar{\lambda}}^G(\lambda, \bar{\lambda}, \sigma, F, C_{\bar{\lambda}}) = C_{\bar{\lambda}} + F \frac{e^{-(\lambda-\bar{\lambda})^2/(2\sigma^2)}}{\sigma\sqrt{2\pi}}. \quad (2)$$

The free parameters are the total flux, F , in $\text{erg} \cdot \text{s}^{-1} \cdot \text{cm}^{-2}$, the width, σ , in \AA .

(vii) Fit the [O II] doublet with a double-Gaussian profile. Because the high resolution of the DEIMOS spectrograph, we are able to resolve the [O II] doublet. The double-Gaussian profile is given by

$$f_{\lambda}(\lambda, \sigma, F, y, C_{\bar{\lambda}}) = C_{\bar{\lambda}} + \frac{F}{\sigma\sqrt{2\pi}} \left[\frac{(1-y)}{e^{\frac{(\lambda-3726)^2}{2\sigma^2}}} + \frac{y}{e^{\frac{(\lambda-3729)^2}{2\sigma^2}}} \right] \quad (3)$$

The line flux ratio is thus given by $F_{3729}/F_{3726} = y/(1-y)$.

For the data observed with VIMOS at resolution $\mathcal{R} \sim 230$, we cannot fit for the y parameter and we fix it to be 0.58, its mean expected value (Pradhan et al. 2006). If we fit a single Gaussian, the fits converge as well. But the width of the line will encompass both lines and it is less convenient to compare it to the width of other lines.

Fig. 1 shows two examples of spectra (one from VVDS-Deep and one from DEEP2) as well as the model fitted to the emission lines. The differences due to the discrepant resolution are clear.

When the fitting fails (e.g., due to masked pixels, high sky residuals), we output in the catalogue the estimates of the continuum C_{λ} and the flux density in the two pixels nearest to the expected line position.

Limitations

We do not correct for the Balmer absorption intrinsic to the underlying stellar continuum, which requires high SNR. In the DEEP2 spectra out of 7,002 with an H β fit, we found two galaxies with a continuum SNR above 10 around the H β lines and a negative flux fitted. This is a small fraction of galaxies where we could be biased in the estimation of the line flux by not accounting for the absorption.

In typical star-forming galaxies, star formation and thus line emission can be more extended than stellar continuum (e.g. Förster Schreiber et al. 2011; Nelson et al. 2013). As a consequence, the use of slit or aperture with a limited size may introduce a bias in the total flux measurements. Nelson et al. (2013) found that, on average, the size of H α -emitting region is 1.3 times larger than the R -band continuum size for strongly star-forming galaxies at $z \sim 1$. The effective size of star-forming galaxies is about 5–10 kpc (in diameter) at $z \sim 1$ (e.g. Colbert et al. 2013; Nelson et al. 2013; Wuyts et al. 2013), and we expect that the arcsec-wide slit used in DEEP2 or VVDS encloses most, if not all, of the line emission. In addition, the DEEP2 team has compared the spatial profiles along the slit for line emission and stellar continuum and no difference was detected (DEEP2 team, private communication).

2.4 Emission line flux limit

As we are interested in the statistics of emission line fluxes, we need to understand the completeness of each line measurement, i.e., whether or not we can detect the line of interest with an SNR of 5 level at the expected wavelength. Ideally, we could determine the line completeness as a function of wavelength (thus redshift) for every individual spectrum, which depends on the observing conditions and the sky-background SED. For simplicity, however, we choose to use a conservative mean flux limit for each survey. We use the exposure time calculators (ETC) from VIMOS and DEIMOS to obtain an estimate of the noise level given the instrumental set up of each survey at 8300Å, centre of the I band at the redder end of the spectrum where the noise is higher. We construct a fake spectrum with two components: a constant continuum (in f_{λ}) and a single emission line with a Gaussian profile. The integral of the spectrum sums to the limiting magnitude. We vary the relative importance of the emission line to the continuum to obtain a set of

spectra that would be observed at the magnitude limit. We fit the emission line using the noise from the ETC and obtain the SNR as a function of line flux. We obtain the following mean SNR 5 flux limits: $f_{\min}^{\text{DEEP2}} = 2.7$, $f_{\min}^{\text{VVDS Deep}} = 1.9$, and $f_{\min}^{\text{VVDS Wide}} = 3.5 \times 10^{-17} \text{ erg} \cdot \text{s}^{-1} \cdot \text{cm}^{-2}$. In practice, to be conservative, we only consider the luminosity bins that are brighter than the flux limits at a given redshift when measuring the LF.

2.5 The emission line catalogues

In total, we detected at least one of the three [O II], H β and [O III] emission lines with SNR > 5 in 35,639 spectra (half the sample). All of them have very secure redshift quality flags VVDS: Zflags \geq 2, DEEP2: ZQUALITY \geq 3. The catalogues are available via the skies and universes data base: <http://projects.ift.uam-csic.es/skies-universes/LFmodels/content/catalogues/>, they are named: `zcat.deep2.dr4.v4.fits` and `VVDS_WIDE_summary.v1.fits`. We report all `VVDS_DEEP_summary.v1.fits` the line fitting results in the catalogues with the following column naming convention: LINE_ELEMENT, IONIZATION_NUMBER, WAVELENGTH, QUANTITY. For example, the [O II] flux is given in the column 'O2_3728_flux' and the error on this quantity is given in the column 'O2_3728_fluxErr'.

3 LUMINOSITY FUNCTIONS

The LF, $\Phi(L)$, measures the number of galaxies (N) per unit volume (V) as a function of luminosity (L):

$$dN = \Phi(L) dL dV. \quad (4)$$

In this section, we define the samples (Section 3.1) used for the LF estimate (presented in Section 3.2).

3.1 Samples design

As the LFs of the three emission lines, [O II], H β and [O III] are spread out in wavelength and redshift, we present here key information on the redshift and luminosity parameter space covered by the data. Fig. 2 shows the redshift and luminosity distribution of the emission lines detected in each survey, together with the associated emission line flux limits as estimated in Section 2.4.

3.1.1 Redshift bins

The redshift range over which lines are detected varies with survey; as shown in Fig. 2. For each line, within its redshift detection limits, we divide the sample into smaller redshift bins to grasp the evolution of the LF. We stop at 9000Å to avoid the hydroxyl forest from the atmosphere. We present the redshift bins in Table 3 for the lines and surveys considered.

In deep pencil beam surveys, the volume covered by the low redshift data is very small, e.g., of order of 10^4 Mpc^3 for $z < 0.18$ for a field of view of few square degrees. The sample variance of any galaxy population is therefore large and thus we do not consider galaxies at $z < 0.18$ in this study.

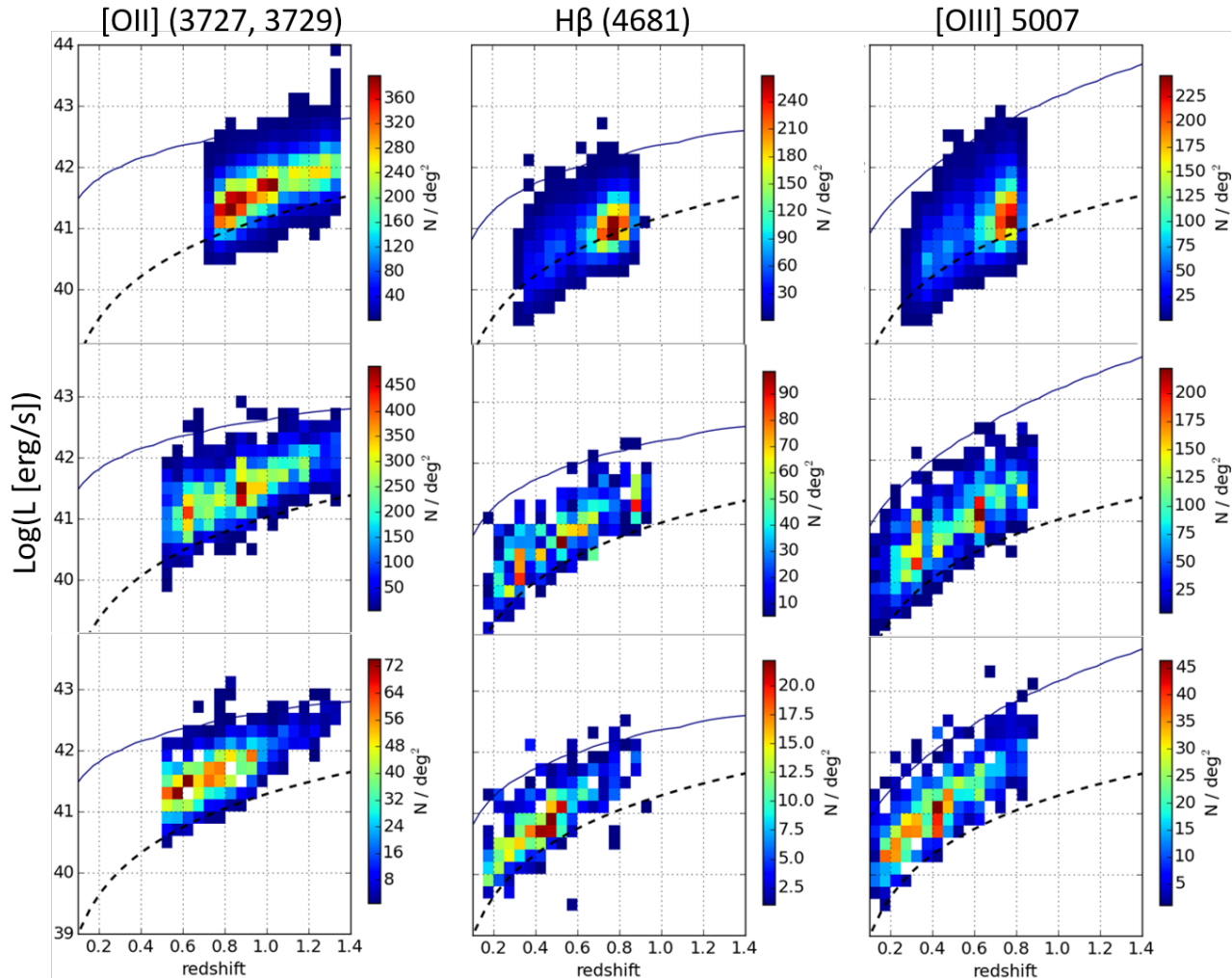


Figure 2. Number density of emitters per square degree as a function of line luminosity and redshift: DEEP2 (first row of panels), VVDS-Deep (second) and VVDS-Wide (third). The dashed lines represent the average 5σ flux limits given in Section 2.4. The density of one emitter per square degree predicted by the best-fitting LFs is represented by the solid blue line. Note that the colour bar range vary from panel to panel. It shows how the detection of the lines is limited in redshift, see Table 3 and text for further details.

3.1.2 Luminosity limits

For each LF we compute its luminosity limit, denoted L_{\min}^{line} , above which the survey is complete. We use a fixed grid of 50 log luminosity bins between 38 and 45 (steps of ~ 0.14 dex). The luminosity limit is constrained by the average 5σ flux limit f_{\min}^{line} , as calculated in Section 2.4, and L_{\min}^{line} has to be greater than $f_{\min}^{\text{line}} 4\pi d_L^2(z_{\max}^{\text{line}})$.

Furthermore, for each LF, we measure the line luminosity at which the weighted number counts distribution (see next section for the description of the weights) peaks, L_{peak} . We find L_{peak} to be always greater than the luminosity limit determined by L_{\min}^{line} . To be conservative, we consider the final luminosity limit L_{\min}^{line} to be 4 times greater than L_{peak} , i.e., we discard the first two bins of luminosity. We report the luminosity limits for all the lines, redshifts and surveys considered in Tables 4- refOIII:LFs:literature.

3.2 LF measurements

3.2.1 Sampling rate corrections

For each galaxy, we correct the observed densities from the target success rate (TSR) and the spectroscopic success rates (SSR). The TSR is the number of targets that were allocated a slit for spectroscopic observation divided by the number of photometric targets down to an apparent magnitude limit. The TSR depends on RA, DEC, magnitudes and for VVDS on the size of the galaxy along the spatial dimension of the slit (see Ilbert et al. 2005). The SSR is the fraction of spectroscopic targets for which the redshift was successfully determined. The SSR depends on RA, DEC, magnitudes, and redshift. To compute an LF for a given survey, considering we are interested in the average volume density over the entire (small) area covered by the survey, we here choose to ignore the variations of the TSR and SSR as a function of the location (though these variations would be important for clustering analysis). Furthermore, we bin the data in narrow redshift bins, and therefore, we neglect the variation of TSR

Table 3. Redshift bins used in the analysis, x means an LF was measured.

Redshift		Line		
min	max	[O II]	H β	[O III]
VVDS				
0.18	0.41		x	x
0.41	0.65		x	x
0.51	0.7	x	x	x
0.56	0.83	x	x	x
0.65	0.84	x	x	x
0.84	1.1	x		
1.1	1.3	x		
DEEP2				
0.33	0.45		x	x
0.45	0.60		x	x
0.60	0.70		x	x
0.7	0.75		x	x
0.75	0.78	x	x	x
0.78	0.83	x	x	
0.83	1.16	x		
1.16	1.30	x		

with galaxy size. VVDS-Deep TSR and SSR are provided through their data base (see Ilbert et al. 2005, for more details). For the VVDS-Wide and DEEP2, we compute them as follows.

We use the targeting photometry to derive the TSR as a function of magnitude. We find that DEEP2 has a TSR around 65% in its field 1 for galaxies with magnitudes $18.5 < R < 22$ and around 60% for magnitudes fainter than 22; see Fig. 3 top panel. For DEEP2 Fields 2, 3, 4, we assume the colour pre-selection was efficient and selected galaxies only at $z > 0.7$, and we use the photometric sample *after* the colour pre-selection as the parent sample. We obtain a TSR $\sim 60\%$. In these fields, we consider only the redshift range $z > 0.7$ in the LF measurements. The TSR of VVDS-Wide is between 10 and 20% down to $i < 22.5$; see Fig. 3 top panel.

To estimate the SSR, we use the photometric redshift catalogues from Ilbert et al. (2006, 2009) and Coupon et al. (2009) to complement the spectroscopic redshift catalogues. These photometric redshift catalogues cover the same area as the spectroscopic surveys. For the SSR, we only account for its dependence on redshift (including colour and magnitude has a negligible effect on our results). For each targeted galaxy, if the survey failed to determine the redshift from the spectroscopy, we use the photometric redshift. We then calculate the SSR as the fraction of galaxies with successful spectroscopic redshift in each redshift bin. The smallest redshift bin used in the LF analysis has a width of $dz = 0.03$ (at $z \sim 0.75$) and the photometric redshift precision is $\sigma_z/(1+z) \sim 0.005(1+0.75)$, which should be sufficient. In a given redshift bin, the sum of the $1/SSR$ therefore represents the expected number of (targeted) galaxies. We determine that DEEP2 has an average $SSR > 80\%$ over the redshift range $0.2 < z < 1.2$, VVDS-Deep has an average $SSR > 80\%$ at $0.4 \lesssim z \lesssim 1.2$, and VVDS-Wide has an SSR around 0.95.

Finally each galaxy with a spectroscopic redshift z_{spec} and an apparent magnitude m receives a weight $1/(\text{TSR}(m) \cdot \text{SSR}(z_{\text{spec}}))$ to account for missed galaxies due to targeting completeness and redshift success rate.

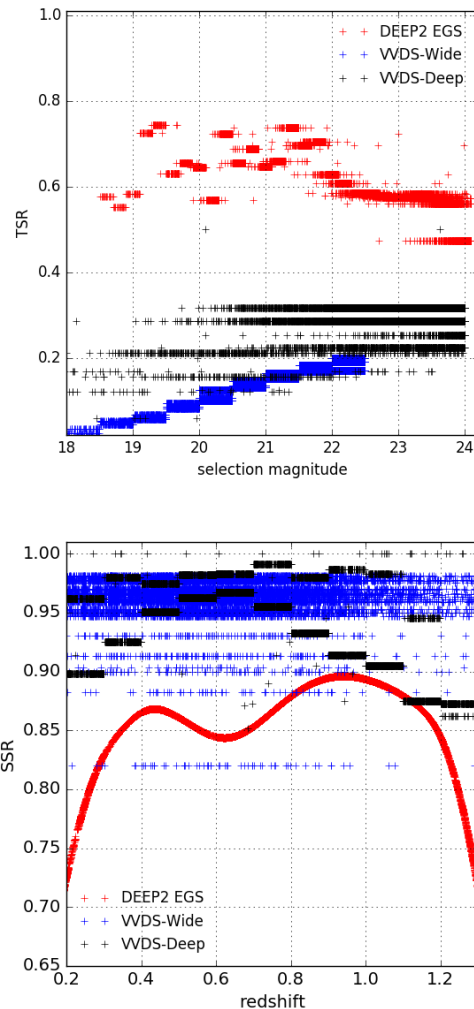


Figure 3. TSR as a function of magnitude (top) and SSR as a function of redshift (bottom). We show the values obtained for the following fields: DEEP2 EGS, VVDS-Deep and VVDS-Wide.

3.2.2 Measurements and redshift evolution

We estimate the LF with the samples described above with the non-parametric V_{max} estimator (Schmidt 1968; Johnston 2011). We measure in total 18 LFs ([O II]: 8, H β : 5, and [O III]: 5) in redshift bins between 0.18 and 1.30. Sample variance errors are estimated using the jackknife technique. Using numerous realizations of the COSMOS and SUBARU Deep Field, Sobral et al. (2015) derived the uncertainty on the emission line LF parameter estimation as a function of volume. For the volumes considered in this analysis (of the order of 10^6 Mpc^3 for each LF), we expect errors induced by cosmic variance to be of order of 10 - 20% (for each LF).

To complement our measurements, we have also gathered from the literature measurement of emission line LFs that cover a volume larger than $\sim 10^4 \text{ Mpc}^3$ and span at least half an order of magnitude in luminosity. For the samples that were re-analysed, we only considered the latest version of the measurement. The sources, the redshift and luminosity distribution of these measurements of is shown

in Table 4 for the [O II] doublet, in Table 5 for the H β line and in Table 6 for the [O III] line. Under this volume constraint, we have not found any measurement of the observed H β emission-line LF alone, i.e. split from [O III] ($\lambda 4959$) and [O III] ($\lambda 5007$). The combination of all the new and previous [O II], H β and [O III] data sets enable the coverage of total volumes of 5, 0.3 and $2 \times 10^7 \text{Mpc}^3$, respectively.

We present our measurements⁹ together with previous measurement from the literature in Figs. 4-6. We observe strong redshift evolution of the LF of all three lines. Over the redshift range $0 \lesssim z \lesssim 2.3$, the characteristic luminosity of [O II] at a given density (e.g., $10^{-4} \text{Mpc}^{-3} \text{dex}^{-1}$) increases with redshift. It also shows that for a fixed [O II] luminosity e.g. $10^{42} \text{erg} \cdot \text{s}^{-1}$ the number density has increased by over a factor of 10 from redshift 0 to 1, consistently with previous studies (e.g., Zhu et al. 2009; Sobral et al. 2015). For the H β and [O III] ($\lambda 5007$), previous works measured the combined LFs, including H β , [O III] ($\lambda 4959$), and [O III] ($\lambda 5007$), and found that the number density of systems at a given luminosity (of the three lines combined) increases with redshift (e.g. Ly et al. 2007; Khostovan et al. 2015; Sobral et al. 2015). From our measurements, for the first time, we can disentangle the contributions of each line to this measurement and find that the number density of strong H β and [O III] emitters increases with redshift, up to $z \sim 0.9$ and $z \sim 1.8$, respectively. We measure that the density of [O III] ($\lambda 5007$) emitting galaxies with $L = 10^{41} \text{erg} \cdot \text{s}^{-1}$ at redshift 0.7 is about twice that of H β emitters $\Phi_{[\text{O III}]}(L = 10^{41} \text{erg} \cdot \text{s}^{-1}, z = 0.7) = 2\Phi_{\text{H}\beta}(L = 10^{41} \text{erg} \cdot \text{s}^{-1}, z = 0.7)$. At the bright end $L > 10^{42} \text{erg} \cdot \text{s}^{-1}$, [O III] ($\lambda 5007$) emitters are 10 times more numerous than H β emitters.

3.3 LF model

To investigate the LFs and their evolution more quantitatively, we explore two analytic models: the Schechter (1976) and Saunders et al. (1990) models, both with parameters explicitly dependent on redshift.

Like broad-band galaxy LFs, the emission line LF is often modelled with a three-parameter Schechter (1976) model:

$$\Phi(L)dL = \phi_* \left(\frac{L}{L_*}\right)^\alpha \exp\left(-\frac{L}{L_*}\right) d\left(\frac{L}{L_*}\right), \quad (5)$$

with Φ_* , L_* and α its parameters representing the density and the luminosity of typical ELGs and the faint-end slope. Recent investigations have found that the [O II] emission line LF when sampled at its brightest end is better represented by a double power-law form (Zhu et al. 2009; Gilbank et al. 2010; Comparat et al. 2015b), which declines less steeply than an exponential as in the Schechter model. This is likely because the Schechter model is most suited for characterizing the stellar mass function, while line emission originates from star formation and the line LF, to the first order, must share the same shape as the SFR function. Recent observations have shown that the SFR function at the high end declines less fast than the Schechter function (Salim & Lee 2012, and references therein). We fit our measurements with

a four-parameter Saunders et al. (1990) model, which is a re-parametrization of a double power-law:

$$\Phi(L)dL = \phi_* \left(\frac{L}{L_*}\right)^\alpha \exp\left[-\left(\frac{\log_{10}(1+L/L_*)}{\sqrt{2}\sigma}\right)^2\right] dL. \quad (6)$$

with Φ_* , L_* , α and σ its parameters representing the density, the luminosity of typical ELGs, the faint-end slope and the width of the transition between the bright and the faint end. Note that these parameters do not have the same meaning with the two models.

For both models, we allow linear redshift dependence for the parameters L_* , Φ_* and α : $L_*(z) = L_*(0)(1+z)^{\beta_L}$, $\Phi_*(z) = \Phi_*(0)(1+z)^{\beta_\Phi}$, $\alpha(z) = \alpha(0)(1+z)^{\beta_\alpha}$ and fit all the measurements over the entire redshift range simultaneously. In all data sets, there is no need to parametrize the redshift dependence of α (data is not sufficient to constrain its eventual evolution). In the Saunders model, we find a transition parameter $\sigma = 0.54 \pm 0.2$ fits the [O II] data well and allows for a smoother transition between the faint and the bright populations. Though this parameter is not well constrained, so in the final analysis, we fix the value $\sigma = 0.54$ for all Saunders fits.

We present the best-fitting models in Table 7 and Figs. 4 (for [O II]), 5 (for H β) and 6 (for [O III]). For all the lines, both L_* and Φ_* increase with redshift, indicating brighter average luminosity and more strong emitters at higher redshift. We also find that for the H β LF, the faint-end slope is similar to that of the H α LF from the literature (e.g., Sobral et al. 2013). Finally, although we find that both models account well for the H β and [O III] data, the Saunders model gives slightly better values of χ^2 . For the [O II] LF, the best Schechter model yields a reduced $\chi^2 = 2.77$ when the best Saunders model has 1.77. We join the conclusions of Zhu et al. (2009) that showed a double power-law accounted well for the observed [O II] LF: the bright end decline of an exponential seems too sharp to model the data.

The global fit presented here is in agreement with former individual results by construction, indeed the data from previous studies is included for the fit. In the literature, Schechter functions are typically fitted on a single redshift bin and on a single galaxy sample. Therefore it is complicated to present a face to face value comparison between each parameter obtained as faint-end slopes, and to a lesser extent cosmological parameters, may vary from a paper to another. We face the same issue when comparing to double power-laws. At redshift $z = 0$, Gilbank et al. (2010) fitted the [O II] LF (L_* , α) = ($10^{41.3} \text{erg} \cdot \text{s}^{-1}$, -1.3) and we find ($10^{41.1} \text{erg} \cdot \text{s}^{-1}$, -1.4), which is very close. Ly et al. (2007) fitted the [O III] LF with a similar faint-end slope as us and they obtain ($\log[L_*(z = 0.42)(\text{erg} \cdot \text{s}^{-1})]$, $\log[L_*(z = 0.83)(\text{erg} \cdot \text{s}^{-1})]$) = (41.7 ± 0.4 , 42.2 ± 0.1) where we have (42.0 ± 0.1 , 42.4 ± 0.1).

Based on the Saunders models, we compute the expected number of sources per deg^2 at a given redshift and luminosity. We show this prediction for a density of 1deg^{-2} as a function of redshift and luminosity for the three lines along with the observed density of data on Fig. 2 (top solid line). Since the surveys used in this analysis are of order of a square degree, this solid line constitutes the bright luminosity limit these surveys can probe within the volume they sample.

⁹ all the measurements are available here <http://projects.ift.uam-csic.es/skies-universes/LFmodels/data>

Table 4. Information about the compilation of the [O II] ($\lambda\lambda 3726, 3729$) LF measurements, ordered by mean redshift. Sources: NB=Narrow-Band; S =spectroscopy. The first set of LFs are derived in this paper. Dashes mean the data are the same as given in the line above. Blank spaces mean we lack the information. The combination of these samples covers $\sim 5 \times 10^7 \text{Mpc}^3$.

Redshift			$\log(\frac{V}{\text{Mpc}^3})$	Area (deg 2)	N	$\log(L [\text{erg} \cdot \text{s}^{-1}])$		Type	Source
mean	min	max				min	max		
0.81	0.78	0.83	5.99	2.78	627	41.8	43.0	S	DEEP2
0.93	0.83	1.03	6.66	2.78	4545	42.0	44.0	S	-
1.23	1.16	1.30	6.60	2.78	926	42.4	44.0	S	-
0.61	0.51	0.70	5.77	0.62	284	41.6	43.0	S	VVDS-Deep
0.74	0.65	0.84	5.88	0.62	373	41.7	43.0	S	-
0.94	0.84	1.10	6.13	0.62	600	42.0	43.0	S	-
0.64	0.51	0.70	6.74	5.79	504	42.8	43.1	S	VVDS-Wide
0.74	0.65	0.84	6.85	5.79	411	42.8	43.1	S	-
0.10	0.03	0.20	7.20	275.00	43155	39.7	42.0	S	Gilbank et al. (2010)
0.15	0.00	0.20	4.63	0.46	39	40.0	41.5	S	Ciardullo et al. (2013)
0.26	0.2	0.32	4.90	0.46	70	40.0	41.5	S	-
0.38	0.32	0.45	5.18	0.46	89	40.5	42.0	S	-
0.50	0.45	0.56	5.26	0.46	76	40.5	42.0	S	-
0.17	0.10	0.24	5.00	48.00	4450	40.5	42.5	S	Comparat et al. (2015b)
0.59	0.5	0.69	5.98		4579	41.0	43.5	S	-
0.78	0.69	0.88	6.10		3951	41.0	43.5	S	-
0.98	0.88	1.09	6.26		1947	41.0	43.5	S	-
1.49	1.34	1.65	6.55		231	42.7	44.0	S	-
0.35			4.38	0.38	112	40.0	41.2	NB	Drake et al. (2013)
0.53			4.63	0.38	83	40.5	41.0	NB	-
1.19			5.31	0.38	981	41.3	42.0	NB	-
1.64			5.48	0.38	27	42.	43.0	NB	-
0.91	0.90	0.92	4.54	0.24	5897	41.5	42.0	NB	Ly et al. (2007)
2.18	2.16	2.20	5.54	10.00	463	42.7	43.3	NB and S	Sobral et al. (2015)
1.47	1.45	1.49	5.83			42.0	42.6	NB and S	Khostovan et al. (2015)
2.25	2.23	2.27	5.79			42.6	42.7	NB and S	-

Table 5. Information about the compilation of the H β LF measurements, ordered by mean redshift, only from this paper. The combination of all the samples covers $\sim 3 \times 10^6 \text{Mpc}^3$.

Redshift			$\log(\frac{V}{\text{Mpc}^3})$	Area (deg 2)	N	$\log(L [\text{erg} \cdot \text{s}^{-1}])$		Type
mean	min	max				min	max	
0.40	0.33	0.45	5.25	0.60	269	40.2	42.5	S
0.52	0.45	0.60	5.57	0.60	360	40.6	42.0	S
0.65	0.60	0.70	5.48	0.60	456	40.7	42.3	S
0.75	0.70	0.78	6.12	2.78	1142	40.9	42.7	S
0.80	0.78	0.83	5.96	2.78	739	41.0	42.7	S

Table 6. Information about the compilation of the [O III] ($\lambda 5007$) ([O III] ($\lambda 4959$) is not included) LF measurements, ordered by mean redshift. Sources: NB=Narrow-Band; S =spectroscopy. The combination of these samples covers $\sim 2 \times 10^7 \text{Mpc}^3$.

Redshift			$\log(\frac{V}{\text{Mpc}^3})$	Area (deg 2)	N	$\log(L [\text{erg} \cdot \text{s}^{-1}])$		Type	Source
mean	min	max				min	max		
0.36	0.33	0.40	4.97	0.60	326	40.5	42.8	S	DEEP2
0.55	0.50	0.60	5.39	0.60	211	40.5	42.8	S	-
0.65	0.60	0.70	5.48	0.60	319	41.0	42.8	S	-
0.74	0.70	0.78	6.12	2.78	550	41.1	42.8	S	-
0.54	0.41	0.65	5.75	0.61	325	40.8	42.2	S	VVDS-Deep
0.41	0.39	0.41	4.09	0.24	2219	39.5	41.3	NB	Ly et al. (2007)
0.50	0.10	0.90	5.79	0.20	401	39.5	41.5	S	Pirzkal et al. (2013)
0.83			5.09	0.38	910	41.0	41.5	NB	Drake et al. (2013)
0.99			5.17	0.38	32	41.5	42.0	NB	-
1.15	0.7	1.5	6.84	1.04	155	41.7	42.7	S	Colbert et al. (2013)
1.85	1.5	2.2	6.85	1.04	54	42.2	43.0	S	-

Table 7. The best-fitting Schechter and Saunders redshift dependent models. For each line and each model, we give the values of the parameters characterizing equations (5) and (6). For Saunders model’s fits we fix σ to 0.54. Models are illustrated in Figs. 4 (for [O II]), 5 (for H β) and 6 (for [O III]).

line	model	$\chi^2/\text{d.o.f}$	$L_*(z)$ [erg \cdot s $^{-1}$] = $L_*(0)(1+z)^{\beta_L}$	$\Phi_*(z)$ [Mpc $^{-3}$] = $\Phi_*(0)(1+z)^{\beta_\Phi}$	$\alpha(z) = \alpha(0)$		
			$\log_{10}(L_*(0))$	β_L	$\log_{10}(\Phi_*(0))$	β_Φ	$\log_{10}(\alpha(0))$
[O II]	Schechter	2.77	$41.1^{+0.02}_{-0.03}$	$2.33^{+0.14}_{-0.16}$	$-2.4^{+0.03}_{-0.03}$	$-0.73^{+0.25}_{-0.29}$	$-1.46^{+0.06}_{-0.05}$
[O II]	Saunders	1.77	$40.1^{+0.02}_{-0.03}$	$1.92^{+0.13}_{-0.16}$	$-1.95^{+0.03}_{-0.03}$	$0.07^{+0.24}_{-0.28}$	$-1.12^{+0.04}_{-0.04}$
H β	Schechter	0.62	$40.88^{+0.05}_{-0.07}$	$2.19^{+0.25}_{-0.32}$	$-3.34^{+0.09}_{-0.12}$	$2.7^{+0.44}_{-0.57}$	$-1.51^{+0.27}_{-0.2}$
H β	Saunders	0.45	$39.7^{+0.06}_{-0.07}$	$1.63^{+0.26}_{-0.34}$	$-2.92^{+0.09}_{-0.11}$	$3.37^{+0.44}_{-0.56}$	$-0.81^{+0.07}_{-0.1}$
[O III]	Schechter	0.61	$41.42^{+0.07}_{-0.09}$	$3.91^{+0.32}_{-0.4}$	$-3.41^{+0.08}_{-0.1}$	$-0.76^{+0.39}_{-0.49}$	$-1.83^{+0.1}_{-0.08}$
[O III]	Saunders	0.56	$40.81^{+0.07}_{-0.09}$	$3.31^{+0.32}_{-0.4}$	$-2.91^{+0.08}_{-0.1}$	$-0.22^{+0.39}_{-0.49}$	$-1.81^{+0.17}_{-0.13}$

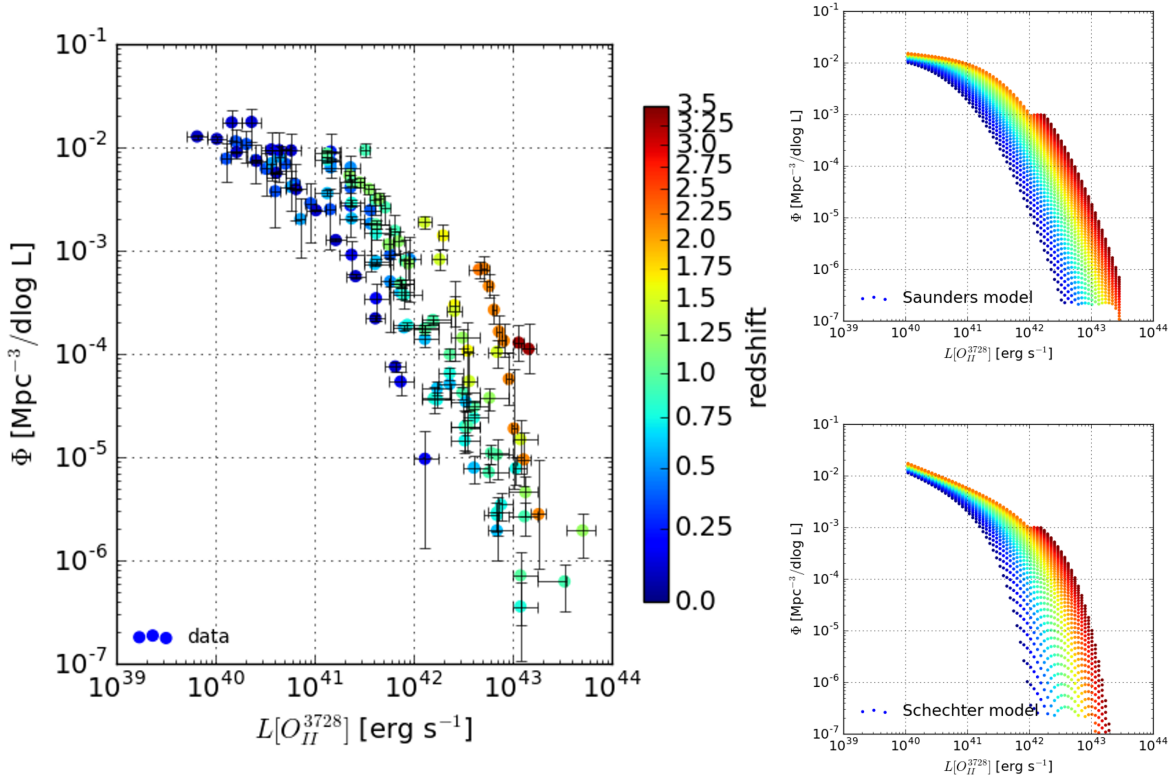


Figure 4. Left: the observed [O II] ($\lambda\lambda 3726, 3729$) LF. Right: the best-fitting Schechter and Saundner model models. Error bars come from jackknife re-sampling for our measurements. The redshift colour coding is the same for all panels.

4 SUMMARY

We have collected the spectroscopic data from two deep surveys (VVDS, DEEP2) and measured the LFs of three emission lines, [O II] ($\lambda\lambda 3726, 3729$), H β ($\lambda 4861$) and [O III] ($\lambda 5007$) at moderate redshifts ($0.2 \lesssim z \lesssim 1.3$) using 35,639 galaxy spectra.

We compiled previous measurements from the literature and performed analytic fitting to the entire data sets of each emission line with both Schechter (1976) and Saunders et al. (1990) models, allowing natural redshift dependence of the parameters L^* and ϕ^* . For all lines, we find previous measurements to be compatible with newer measurements and they can be modelled together with a natural redshift evolution. This compilation of the literature along with the new measurements reaches large volumes: $\sim 5 \times 10^7$

Mpc 3 for [O II], $\sim 3 \times 10^6$ Mpc 3 for H β , $\sim 2 \times 10^7$ Mpc 3 for [O III] ($\lambda 5007$).

We find that for all the three lines, the characteristic luminosity and density increase with redshift. Using the Schechter model over the redshift ranges considered, we find that, for [O II] emitters, the characteristic luminosity $L_*(z = 0.5) = 3.2 \times 10^{41} \text{ erg} \cdot \text{s}^{-1}$ increases by a factor of 2.7 ± 0.2 from $z=0.5$ to $z=1.3$, for H β emitters $L_*(z = 0.3) = 1.3 \times 10^{41} \text{ erg} \cdot \text{s}^{-1}$ by a factor of 2.0 ± 0.2 from $z=0.3$ to $z=0.8$, and for [O III] emitters $L_*(z = 0.3) = 7.3 \times 10^{41} \text{ erg} \cdot \text{s}^{-1}$ by a factor of 3.5 ± 0.4 from $z=0.3$ to $z=0.8$. It indicates that on average, the emitters are more numerous and luminous at higher redshift.

This measurement is crucial for the development of truthful ELGs mock catalogues based on N -body simula-

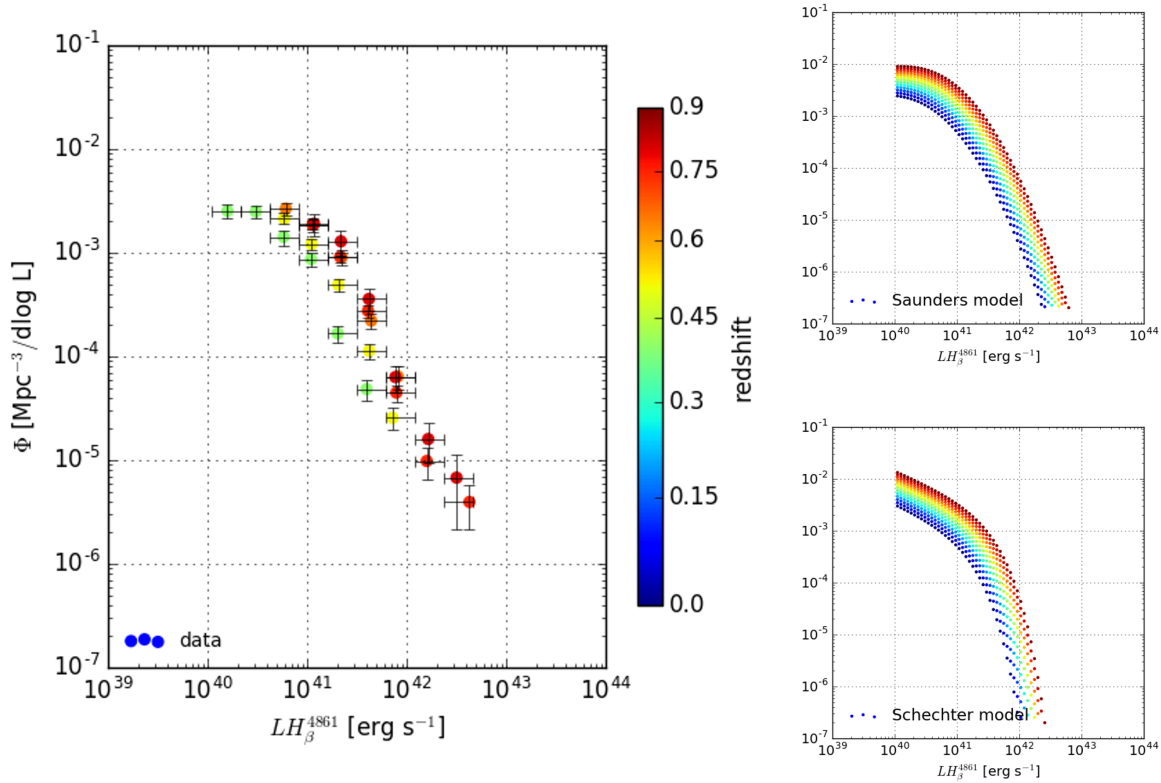


Figure 5. Same as Fig. 4 for the $H\beta$ ($\lambda 4861$) LF.

tions and semi-analytical models (e.g. Gonzalez-Perez et al. 2014; Orsi et al. 2014). In the future, we hope to compare such mock catalogues with semi-analytical models of galaxy formation with these measurements and hereby obtain a better understanding of the links between line luminosity, SFR and dust in ELGs at redshift one. In this aim, we will study in the near future the conditional emission line LFs and line ratios distributions. On the longer term, we aim to understand precisely the place of this ELG population within the global paradigm of galaxy formation and evolution. This is utmost important to make sure the planned ELG-BAO measurements will not be affected by systematics due to selection effect.

Finally, our data and measurements is made publicly available and we provide a PYTHON package to mine further the information available in this data set. The framework developed is flexible so that any new data set can be seamlessly folded into the luminosity function fits.

References

- Anderson L. et al., 2014, MNRAS, 441, 24
 Bayliss K. D., McMahon R. G., Venemans B. P., Ryan-Weber E. V., Lewis J. R., 2011, MNRAS, 413, 2883
 Bolton A. S. et al., 2012, AJ, 144, 144
 Ciardullo R. et al., 2013, ApJ, 769, 83
 Colbert J. W. et al., 2013, ApJ, 779, 34
 Cole S. et al., 2005, MNRAS, 362, 505
 Comparat J. et al., 2015a, ArXiv e-prints 1509.05045
 Comparat J. et al., 2015b, A&A, 575, A40
 Coupon J. et al., 2009, A&A, 500, 981
 Cucciati O. et al., 2012, A&A, 539, A31
 Drake A. B. et al., 2013, MNRAS, 433, 796
 Eisenstein D. J. et al., 2005, ApJ, 633, 560
 Faber S. M. et al., 2003, in Society of Photo-Optical Instrumentation Engineers (SPIE) Conference Series, Vol. 4841, Instrument Design and Performance for Optical/Infrared Ground-based Telescopes, Iye M., Moorwood A. F. M., eds., pp. 1657–1669
 Förster Schreiber N. M., Shapley A. E., Erb D. K., Genzel R., Steidel C. C., Bouché N., Cresci G., Davies R., 2011, ApJ, 731, 65
 Freedman W. L., Madore B. F., 2010, ARA&A, 48, 673
 Frieman J. A., Turner M. S., Huterer D., 2008, ARA&A, 46, 385
 Gilbank D. G., Baldry I. K., Balogh M. L., Glazebrook K., Bower R. G., 2010, MNRAS, 405, 2594
 Gonzalez-Perez V., Lacey C. G., Baugh C. M., Lagos C. D. P., Helly J., Campbell D. J. R., Mitchell P. D., 2014, MNRAS, 439, 264
 Ilbert O. et al., 2006, A&A, 457, 841
 Ilbert O. et al., 2009, ApJ, 690, 1236
 Ilbert O. et al., 2005, A&A, 439, 863
 Johnston R., 2011, A&A Rev., 19, 41
 Kennicutt, Jr. R. C., 1998, ARA&A, 36, 189
 Kewley L. J., Geller M. J., Jansen R. A., 2004, AJ, 127, 2002

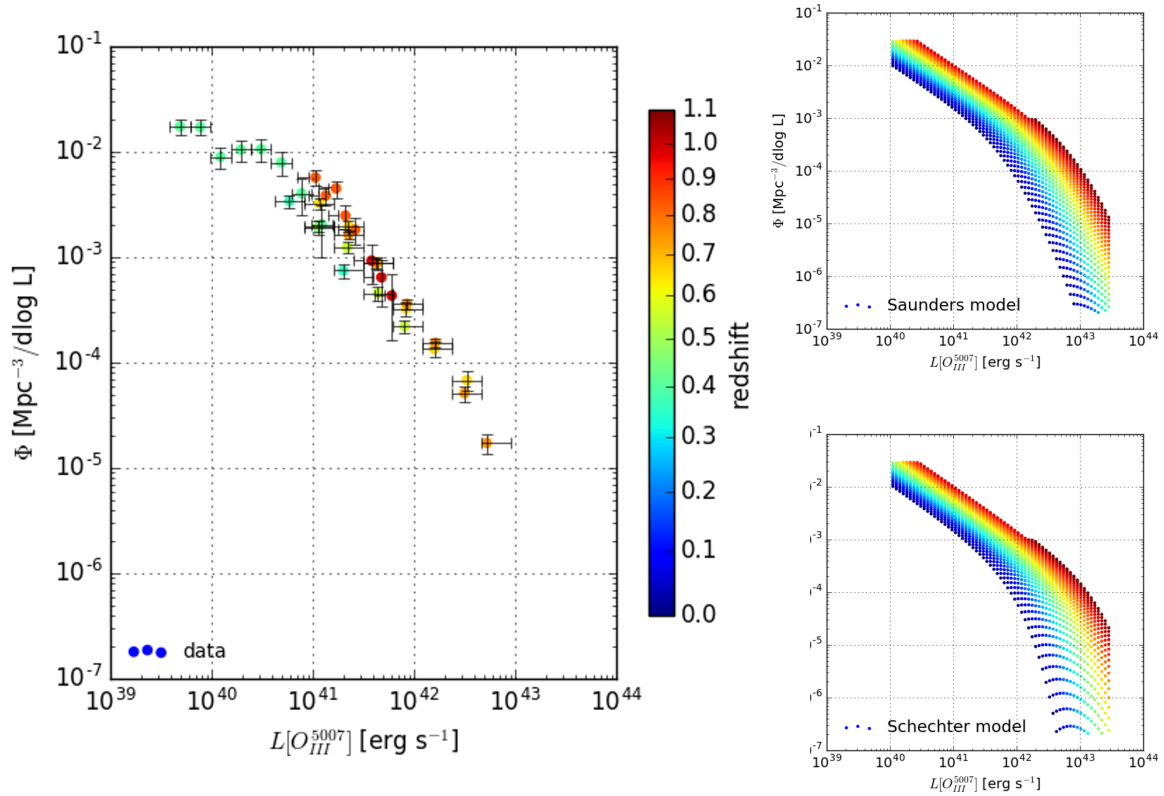


Figure 6. Same as Fig. 4 for the [O III] ($\lambda 5007$) LF.

Khostovan A. A., Sobral D., Mobasher B., Best P. N., Smail I., Stott J. P., Hemmati S., Nayyeri H., 2015, *MNRAS*, 452, 3948

Le Fèvre O. et al., 2013, *A&A*, 559, A14

Le Fèvre O. et al., 2003, in *Society of Photo-Optical Instrumentation Engineers (SPIE) Conference Series*, Vol. 4841, Instrument Design and Performance for Optical/Infrared Ground-based Telescopes, Iye M., Moorwood A. F. M., eds., pp. 1670–1681

Luridiana V., Morisset C., Shaw R. A., 2015, *A&A*, 573, A42

Ly C. et al., 2007, *ApJ*, 657, 738

McCracken H. J. et al., 2003, *A&A*, 410, 17

Moustakas J., Kennicutt, Jr. R. C., Tremonti C. A., 2006, *ApJ*, 642, 775

Myers A. D. et al., 2015, *ApJS*, 221, 27

Nelson E. J. et al., 2013, *ApJ*, 763, L16

Newman J. A. et al., 2013, *ApJS*, 208, 5

Oke J. B., Gunn J. E., 1982, *NASA STI/Recon Technical Report N*, 83, 11000

Orsi Á., Padilla N., Groves B., Cora S., Tecce T., Gargiulo I., Ruiz A., 2014, *MNRAS*, 443, 799

Palanque-Delabrouille N. et al., 2016, *A&A*, 589, C2

Pirzkal N. et al., 2013, *ApJ*, 772, 48

Planck Collaboration et al., 2014, *A&A*, 571, A11

Pradhan A. K., Montenegro M., Nahar S. N., Eissner W., 2006, *MNRAS*, 366, L6

Prakash A., Licquia T. C., Newman J. A., Rao S. M., 2015, *ApJ*, 803, 105

Raichoor A. et al., 2016, *A&A*, 585, A50

Ross A. J., Percival W. J., Manera M., 2015, *MNRAS*, 451, 1331

Salim S., Lee J. C., 2012, *ApJ*, 758, 134

Saunders W., Rowan-Robinson M., Lawrence A., Efstathiou G., Kaiser N., Ellis R. S., Frenk C. S., 1990, *MNRAS*, 242, 318

Schechter P., 1976, *ApJ*, 203, 297

Schmidt M., 1968, *ApJ*, 151, 393

Sobral D., Best P. N., Matsuda Y., Smail I., Geach J. E., Cirasuolo M., 2012, *MNRAS*, 420, 1926

Sobral D. et al., 2015, *MNRAS*, 451, 2303

Sobral D., Smail I., Best P. N., Geach J. E., Matsuda Y., Stott J. P., Cirasuolo M., Kurk J., 2013, *MNRAS*, 428, 1128

Suzuki N. et al., 2012, *ApJ*, 746, 85

Thomas D. et al., 2013, *MNRAS*, 431, 1383

Tonegawa M. et al., 2015, *ArXiv e-prints* 1502.07900

Vargas-Magaña M. et al., 2014, *MNRAS*, 445, 2

Wuyts S. et al., 2013, *ApJ*, 779, 135

Zhu G., Moustakas J., Blanton M. R., 2009, *ApJ*, 701, 86

ACKNOWLEDGEMENTS

JC and FP acknowledge support from the Spanish MICINN Consolider-Ingenio 2010 Programme under grant Multi-Dark CSD2009-00064, MINECO Centro de Excelencia

Severo Ochoa Programme under the grants SEV-2012-0249, FPA2012-34694, and the projects AYA2014-60641-C2-1-P and AYA2012-31101. GY acknowledges financial support from MINECO (Spain) under project number AYA2012-31101 and AYA2015-63810. PN acknowledges the support of the Royal Society through the award of a University Research Fellowship, the European Research Council, through receipt of a Starting Grant (DEGAS-259586), and the support of the Science and Technology Facilities Council (ST/L00075X/1). TD and JPK acknowledge support from the LIDA ERC advanced grant. AR acknowledges funding from the P2IO LabEx (ANR-10-LABX-0038) in the framework Investissements d'Avenir (ANR-11-IDEX-0003-01) managed by the French National Research Agency (ANR). EJ and LT acknowledge the support of CNRS and the Labex OCEVU. This work has been carried out thanks to the support of the OCEVU Labex (ANR-11-LABX-0060) and the A*MIDEX project (ANR-11-IDEX-0001-02) funded by the "Investissements d'Avenir" French government programme managed by the ANR.